Supporting Information

In Situ Encapsulation of Core–Shell–Structured Co@Co_3O_4 into Nitrogen-Doped Carbon Polyhedra as a Bifunctional Catalyst for Rechargeable Zn–Air Batteries

Ziyang Guo,[a] Fengmei Wang, [a] Yuan Xia, [b] Jinli Li, [a] Andebet Gedamu Tamirat, [b] Yanru Liu, [a] Lei Wang, [a] Yonggang Wang*, [b] Yongyao Xia, [b]*

a Key Laboratory of Eco-chemical Engineering, Ministry of Education, College of Chemistry and Molecular Engineering, Qingdao University of Science and Technology, Qingdao 266042, China.

b Department of Chemistry and Shanghai Key Laboratory of Molecular Catalysis and Innovative Materials, Institute of New Energy, Fudan University. Shanghai 200433, China.

---

* Corresponding author. Tel & Fax: 0086-21-51630318
E-mail address: *ygwang@fudan.edu.cn; inorchemwl@126.com*

Material Preparation

Synthesis of ZIF-67 In a typical synthesis procedure, 4.32 g of $Co(NO_3)_3 \cdot 6H_2O$ and 9.75 g of 2-methylimidazole were each added into methanolic solution (300 mL) at room temperature. The former solution was poured into the 2-methylimidazole solution with vigorous stirring. The mixture solution was stirred for 10 mins and then kept for 24 h. The violet solid product was separated by centrifugation and washed with methanol several times, followed by vacuum drying at 100 ^{o}C for overnight. After drying at 100 °C, the bright purple powder of ZIF-67 was obtained.

Co@NC-T preparation The resulting ZIF-67 was directly transferred into a furnace and was heated at different high temperatures (T =700, 800, 900 and 1000 °C, respectively) with heating rate of 10 ^{o}C min^{-1} under an Ar atmosphere for 2 h to form four kinds of powders. The obtained samples are designated as Co@NC-T.

Preparation of alkaline gel solution 0.5g polyvinyl alcohol (M_w=85,000~124,000) was dissolved in 20 mL deionized water at 20 °C under stirring. 2g of KOH was added into the solution. The mixture solution was then heated to 90 °C and kept stirring until the solution became clear. The content of KOH is 0.0357 mol and the obtained solution volume is ~10 ml. Hence, the concentration of KOH in the gel electrolyte is 3.60 M.

Electrochemical characterization

Measurement of Electrocatalytic performances of catalysts towards ORR and ORR: Electrocatalytic ORR and OER measurements were performed in a three-electrode glass cell. The data were recorded using a CHI 660 D bipotentiostat (Shanghai Chen Hua instrument co., LTD, China). The synthesized Co@Co_3O_4@NC-T, commercial Pt/C (20 wt% Pt on carbon black) and RuO_2 were directly used as working electrode for electrochemical characterizations. The reference electrode was Hg/HgO in 1 M KOH solution, and the counter electrode was platinum film. The current density was normalized to the geometrical surface area and the measured potentials vs. Hg/HgO were converted to a reversible hydrogen electrode (RHE) scale according to the Nernst equation ($E_{RHE} = E_{Hg/HgO} + 0.059 \times pH + 0.098$). A flow of O_2 was maintained over the electrolyte (0.1 M KOH) during the recording of electrochemical data in order to ensure the O_2/H_2O equilibrium at 1.23 V vs. RHE. Cyclic voltammograms (CVs) were performed with the scan rate at 5 mV s^{-1}, and working electrodes were scanned for several times until stabilization before CV data were collected. The linear sweep voltammograms (LSVs) were conducted with the scan rate of 5 mV s^{-1}. The working electrodes were scanned for several times until the signals were stabilized, then LSV data were collected, corrected for the iR contribution within the cell. The Tafel slope was calculated according to Tafel equation as follows:

$$\eta = b \cdot log(j/j_0)$$

where η denotes the overpotential, b denotes the Tafel slope, j denotes the current density, and j_0 denotes the exchange current density. The onset potentials were determined based on the beginning of the linear region in Tafel plots. The overpotential was calculated as follows:

$$\eta = E\ (vs.\ RHE)\text{-}1.23$$

Considering O_2/H_2O equilibrium at 1.23 V *vs.* RHE.

On the basis of RDE data, the electron transfer number per oxygen molecule involved in oxygen reduction can be determined by Koutechy-Levich equation (ref. S1 and 2):

$$1/j = 1/j_k + 1/\mathrm{B}w^{1/2}\ (1)$$

where j_k is the kinetic current and ω is the electrode rotating rate. B is determined from the slope of the Koutechy-Levich (K-L) plots according to the Levich equation as given below:

$$\mathrm{B} = 0.2\mathrm{nF}(D_{O2})^{2/3}\upsilon^{-1/6}\ C_{O2}\ (2)$$

where n represents the transferred electron number per oxygen molecule. F is Faraday constant (F = 96485 C mol^{-1}). D_{O2} is the diffusion coefficient of O_2 in 0.1 M KOH (D_{O2} = 1.9 × 10-5 cm^2 s^{-1}). υ is the kinetic viscosity (υ = 0.01 cm^2 s^{-1}). C_{O2} is the bulk concentration of O_2 ($C_{O2} = 1.2 \times 10^{-6}$ mol cm^{-3}). The constant 0.2 is adopted when the rotation speed is expressed in rpm.

Preparation of working electrodes: Firstly, the active material (~4 mg for $Co@Co_3O_4@NC$-*T*) was dispersed in 1 mL of water/ethanol (*v*/*v*: 2/1). Then, 120 μL Nafion (5 wt% aqueous solution, Sigma Aldrich) was added to the above solution under sonication for at least 2 h to form a homogeneous catalyst ink solution. After that, 20 μL ink solution was carefully coated onto a glassy carbon electrode (GC, 5 mm in diameter). And it was finally dried in the air naturally to obtain a uniform thin film. The catalyst loadings were ∼0.36 mg cm^{-2}. The commercial Pt/C (20 wt% Pt on carbon black) and RuO_2 were also employed to prepare the working electrode at the same condition for comparison.

Preparation of air catalytic electrode: Firstly, acetylene black (AB) and poly (tetrafluoroethylene) (PTFE) binder was dispersed in isopropanol to form slurry with a weight ration of 6:4 (AB: PTFE). Next, the slurry (AB + PTFE) was rolled into a membrane with a diameter of 14 mm, and then slightly pressed on the Ni foam to form waterproof layer under the pressure of 5 MPa. After that, with the same way, the slurry (catalyst+KB (Ketjenblack)+PTFE) was rolled into a membrane with a weight ration of 6:3:1 (catalyst: KB: PTFE) and then pressed on the surface of the waterproof layer under the pressure of 40 MPa to form air catalytic cathode. The total mass loading of catalyst in the air cathode is around 1.5~2.0 mg/cm^2. The coated electrode was dried for 12 h at 120 ^{o}C under vacuum to remove residual solvent.

Preparation of Zn–Air Batteries: Zn-air batteries were assembled with a home-made Zn–air cell using a prepared catalyst cathode. The battery performance was evaluated by continuous discharge–charge experiments performed under ambient air conditions (oxygen supplied only from the environment, without additional O_2 sources) using an alkaline aqueous electrolyte of 6 M KOH and a polished zinc plate as the anode. LAND cycler (Wuhan Land Electronic Co. Ltd.) was used for electrochemical investigation.

The mechanical recharge process: Firstly, a Zn–air battery with Co@Co_3O_4@NC-900 catalyst was discharged at a current density of 5 mA cm^{-2} with a fixed time of 20 h. After that, the cell was disassembled in ambient air. Then, the used Zn anode and electrolyte were replaced by the new Zn plate and 6 M KOH solution, respectively. Moreover, the Co@Co_3O_4@NC-900-based cathode was washed with water and ethanol at room temperature. Next, the battery was reassembled by using the new Zn anode, 6 M KOH solution and the washed Co@Co_3O_4@NC-900-based cathode.

Finally, this Zn–air battery continued to be discharged at a current density of 5 mA cm^{-2} with another fixed time of 20 h.

Characterization instrumentation.

XRD measurements were performed on a Bruker D8 Focus power X-ray diffractometer with Cu $K_{\square}$ radiation. SEM investigations were conducted using a JSM-6390 microscope from JEOL. Transmission electron microscopy (TEM) experiments were conducted using a JEOL 2011 microscope (Japan) operated at 200 kV. The surface of as-prepared sample was characterized by Raman spectroscopy (LABRAM-1B). Specific surface areas were calculated by the Brunaure– Emmert–Teller method. Pore volumes and sizes were estimated from the pore-size distribution curves from the adsorption isotherms using the Barrett–Joyner–Halenda method. X-ray photoelectron spectroscopy (XPS) was conducted with a Thermo Escalab 250 equipped with a hemispherical analyzer and using an aluminum anode as a source. Power electronic conductivity investigation with the pressure of 4 MPa was performed on a 4-pole conductivity instrument for powder materials (Powder Resistivity Meter, FZ-2010, Changbao Analysis Co., Ltd, Shanghai, China).

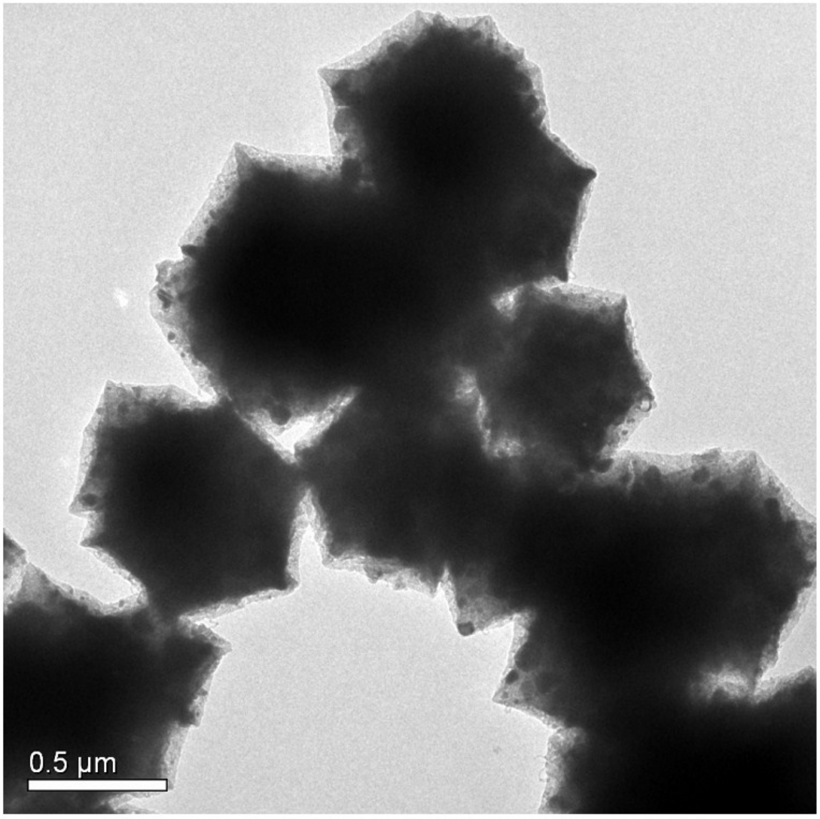

Figure S1 TEM image of as-synthesized Co@NC-900.

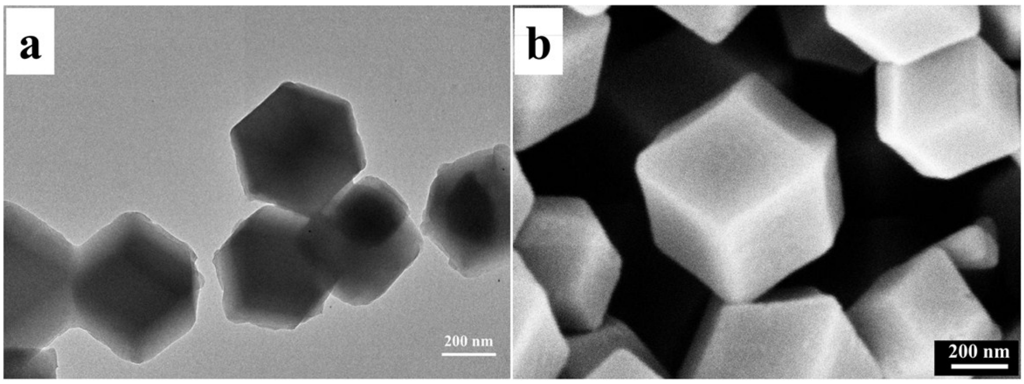

Figure S2 (a) TEM and SEM images of as-synthesized ZIF-67.

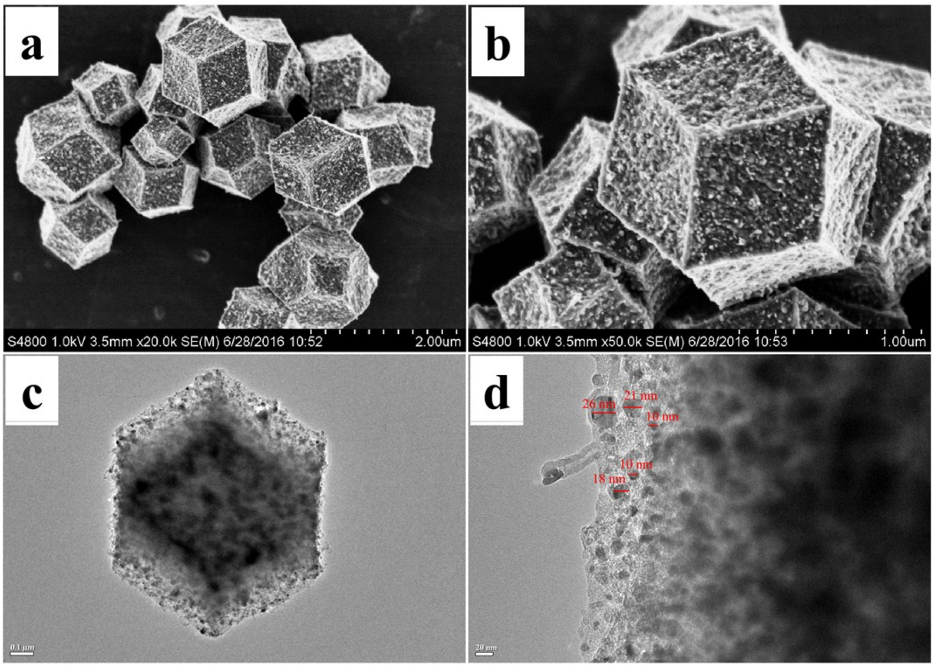

Figure S3 SEM and TEM images of Co@Co_3O_4@NC-700 with different magnifications.

It can be observed from **Figure S3a** and **b** that Co@Co_3O_4@NC-700 exhibits a polyhedral morphology. In addition, the TEM images of Co@Co_3O_4@NC-700 further reveal that it has a core-shell structure, in which Co@Co_3O_4 nanoparticles with the size of 10~26 nm (black dots) are homogenously embedded in the carbon framework (gray matrix; **Figure S3c** and **d**). Furthermore, few CNTs can be found that are wrapping the polyhedral (**Figure S3d**).

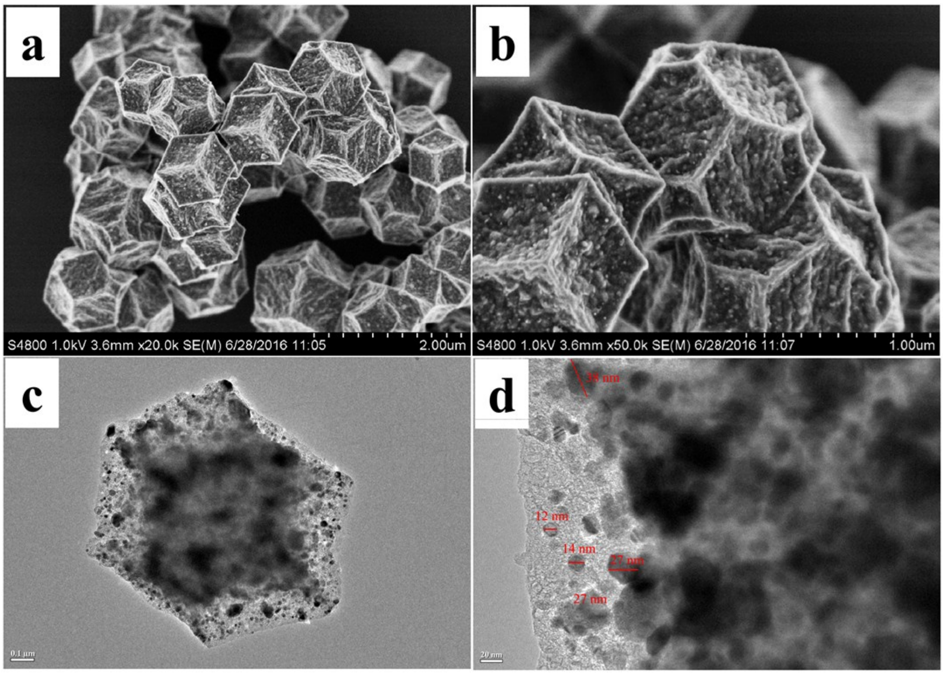

Figure S4 SEM and TEM images of Co@Co_3O_4@NC-800 with different magnifications.

It can be seen from **Figure S4a** and **b** that Co@Co_3O_4@NC-800 also exhibits a polyhedral morphology. **Figure S4c** and **d** show that the Co@Co_3O_4 nanoparticles with the larger size of 12~38 nm (black dots) are still uniformly embedded in the carbon framework (gray matrix) for Co@Co_3O_4@NC-800, which indicates that the temperature rise can lead to the aggregation of Co@Co_3O_4 particles, well consistent with the XRD results (**Figure 3a**).

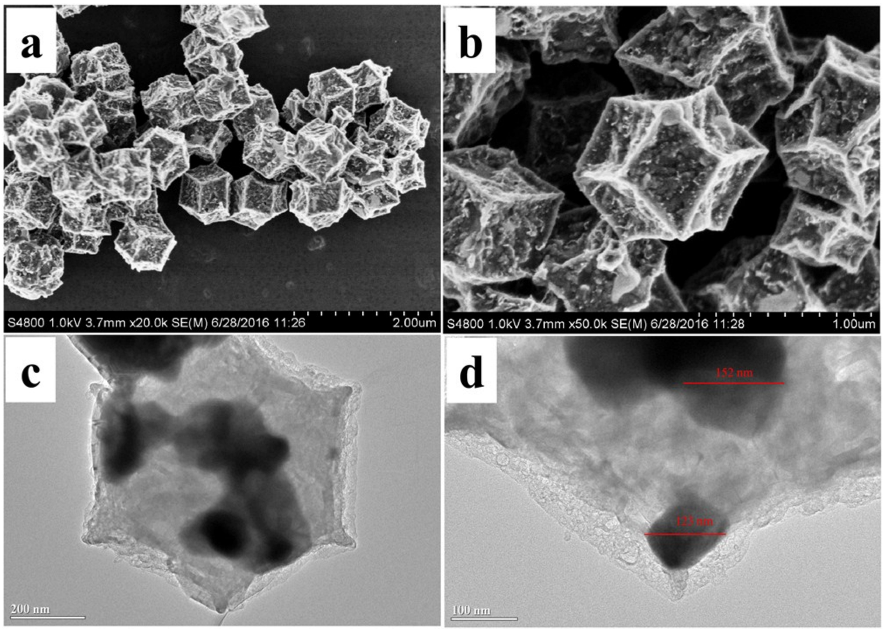

Figure S5 SEM and TEM images of Co@Co_3O_4@NC-1000 with different magnifications.

As shown in **Figure S5a** and **b**, Co@Co_3O_4@NC-1000 exhibits twisted polyhedral morphology, due to the large framework shrinkage at high temperature. Moreover, the Co@Co_3O_4 particles (black dots) in the carbon framework (gray matrix) for Co@Co_3O_4@NC-1000 are obviously aggregated and their sizes increse to > 120 nm (**Figure S5c** and **d**), in good agreement with the results of XRD (**Figure 3a**).

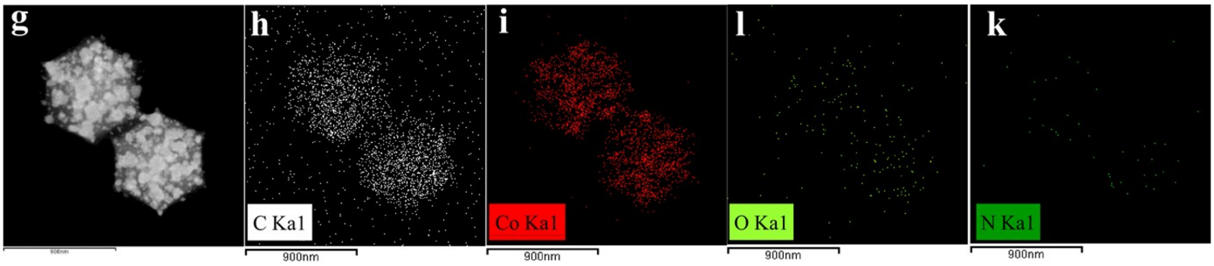

Figure S6 TEM image of Co@Co_3O_4@NC-900 (left) and the corresponding EDX mapping images of C, Co, O and N elements.

Energy-dispersive X-ray (EDX) mapping was further used to investigate the distribution and composition of Co@Co_3O_4@NC-900 composite. As shown in **Figure S6**, the co-existence of C, Co, O and N species can be found on the surface of Co@Co_3O_4@NC-900. Moreover, it can be further observed from **Figure S6** that Co, O and N species are uniformly distributed in the carbon matrix.

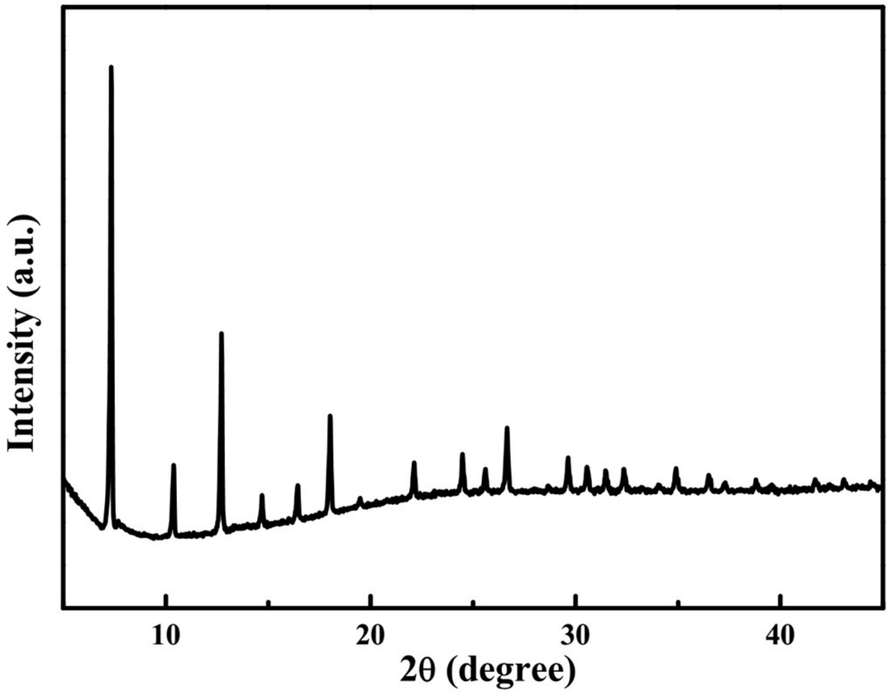

Figure S7 XRD pattern of as-synthesized ZIF-67

As shown in **Figure S7**, all of the main XRD diffraction peaks are attributed to ZIF-67, indicating the successful synthesis of ZIF-67.

Table S1 Electronic conductivities of Co@Co_3O_4@NC-700, Co@Co_3O_4@NC-800, Co@Co_3O_4@NC-900 and Co@Co_3O_4@NC-1000 powders.

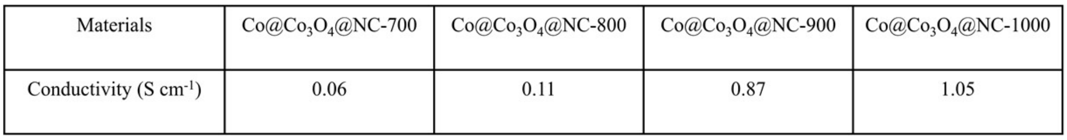

Materials	Co@Co_3O_4@NC-700	Co@Co_3O_4@NC-800	Co@Co_3O_4@NC-900	Co@Co_3O_4@NC-1000
Conductivity (S cm^{-1})	0.06	0.11	0.87	1.05

The electronic conductivities of these materials measured at the pressure of 4 MPa are also summarized in **Table S1**. As shown in **Table S1**, the electronic conductivity of Co@Co_3O_4@NC-700, Co@Co_3O_4@NC-800, Co@Co_3O_4@NC-900 and Co@Co_3O_4@NC-1000 are 0.06, 0.11, 0.87 and 1.05 S cm^{-1}, respectively, further demonstrating that the higher graphitization can lead to the higher electrical conductivity.

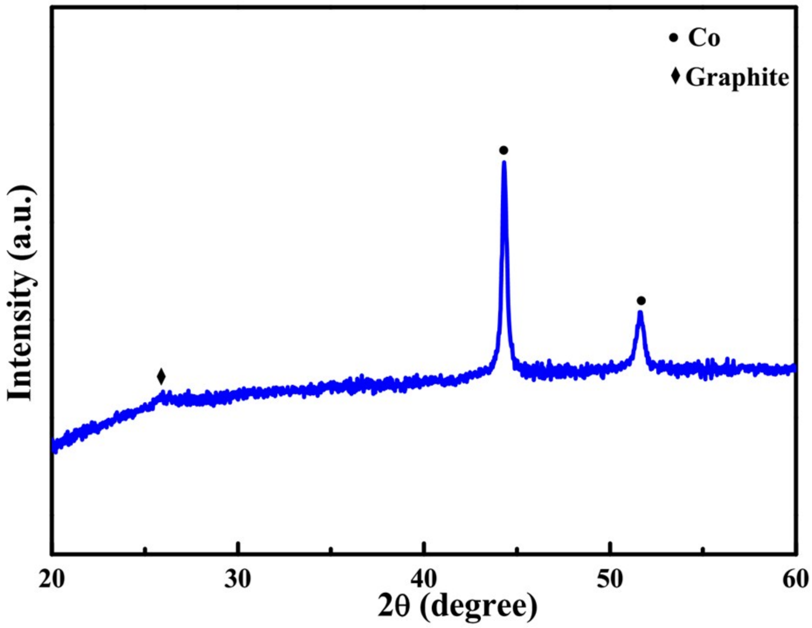

Figure S8 The XRD pattern of as-prepared Co@NC-900.

As shown in **Figure S8**, the XRD analyses of Co@NC-900 shows a broad peak with maxima at 26° originating from the (002) planes of graphitic carbon. Apart from the above peak, there are only two peaks appearing at 44° and 52° which are indexed to the (111) and (200) reflections of face-centered (fcc) Co. Compared with Co@Co_3O_4@NC-900 (**Figure 3a**), no extra peak assigned to the cubic Co_3O_4 spinel phase appears in the XRD pattern of Co@NC-900, further demonstrating that the Co_3O_4 layer is mainly formed during the controlled thermal oxidation process.

Table S2 Porosity parameters of Co@Co_3O_4@NC-700, Co@Co_3O_4@NC-800, Co@Co_3O_4@NC-900 and Co@Co_3O_4@NC-1000. S_{BET}: BET surface area; S_{micro}: surface area of micropores calculated by the t-plot method; V_{total}: total pore volume; V_{micro}: pore volume of micropores.

Sample	S_{BET} (m^2g^{-1})	S_{micro} (m^2g^{-1})	V_{tot} (cm^3g^{-1})	V_{micro} (cm^3g^{-1})	Pore size (nm)
Co@Co_3O_4@NC-700	306.0	243.8	0.125	0.102	3.31
Co@Co_3O_4@NC-800	206.4	160.3	0.110	0.069	3.31
Co@Co_3O_4@NC-900	256.9	193.7	0.145	0.083	3.34
Co@Co_3O_4@NC-1000	74.3	21.4	0.102	0.012	3.35

As listed in **Table S2**, Co@Co_3O_4@NC-900 shows the largest total pore volume (0.145 cm^3 g^{-1}) among four calcined catalyts and its Brunauer–Emmett–Teller (BET) surface area (257 m^2 g^{-1}) is also obviously much higher than that of Co@Co_3O_4@NC-800 (206 m^2 g^{-1}) and Co@Co_3O_4@NC-1000 (74 m^2 g^{-1}), but only slightly lower than that of Co@Co_3O_4@NC-700 (306 m^2 g^{-1}). It is well known that the framework shrinkage and the particle aggregation of one sample can inevitably lead to the decrease of the BET surface area. When the calcination temperature increases from 700 to 1000 °C, the framework shrinkage of carbon polyhedra and the aggregation of Co particles in Co@Co_3O_4@NC-*T* become more and more serious. Hence, the Co@Co_3O_4@NC-700 exhibits the highest BET surface area. On the other hand, more and more oxygen-containing functional groups will be changed into CO_2 and other gases as the temperature rapidly rises. These gases will go out and produce many pores in the carbon framework which can increase the BET surface area. In addition, the total pore volume of the Co@Co_3O_4@NC-900 is obviously higher than these of the Co@Co_3O_4@NC-700 and the Co@Co_3O_4@NC-800, which further confirm the above mechanism. Due to the synergy of the above two reasons, the Co@Co_3O_4@NC-900 has a larger BET surface area as compared with the Co@Co_3O_4@NC-800 but lower than the Co@Co_3O_4@NC-700. Additionally, it can be seen from **Table S2** that Co@Co_3O_4@NC-700, Co@Co_3O_4@NC-800, Co@Co_3O_4@NC-900 and Co@Co_3O_4@NC-1000 exhibit the micropores surface area of 243, 160, 194 and 21 m^2 g^{-1}, respectively.

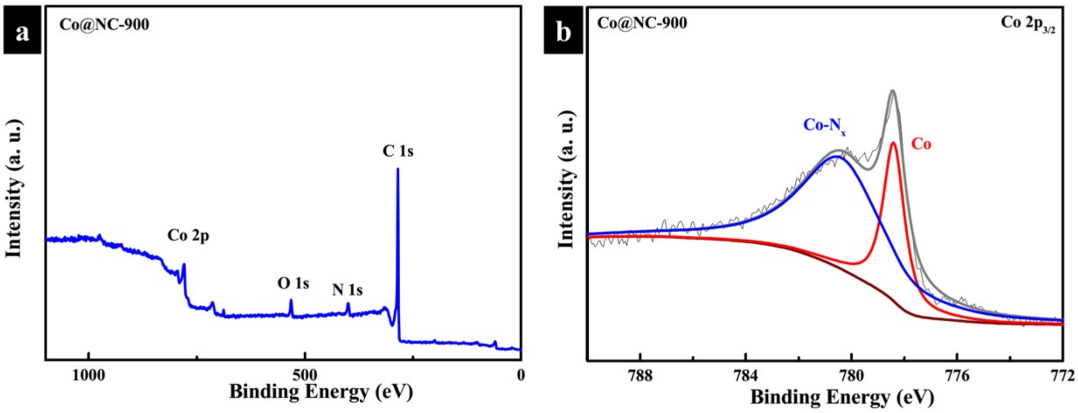

Figure S9 (**a**) Full XPS spectra and (b) High-resolution Co $2p_{3/2}$ XPS spectra of Co@NC-900.

As shown in **Figure S9a**，full XPS spectra of Co@NC-900 also revealed the presence of C, N, O, and Co of Co@NC-900. The C 1s peak centered at 284.7 eV is the typical graphitic carbon peak. The intensity of O 1s peak in Co@NC-900 is much lower than that of Co@Co_3O_4@NC-900 (**Figure 4a**), confirming the formation of metal oxide in Co@Co_3O_4@NC-900. The high-resolution Co $2p_{3/2}$ XPS spectrum of Co@NC-900 was further deconvoluted into two assumed species: Co (~779 eV) and CoN_x (~781.5 eV) (**Figure S9b**). Interestingly, it can be detected from **Figure S9b** that only a sharp metallic Co $2p_{3/2}$ peak and a broad peak attributed to CoN_x appeared in Co@NC-900 while Co@Co_3O_4@NC-900 showed a clear Co $2p_{3/2}$ peak at 780 eV which is assigned to Co_3O_4 (**Figure 4b**), further demonstrating the formation of well-characterized Co_3O_4 in Co@Co_3O_4@NC-900.

Table S3 XPS Spectra Analysis for Co@Co_3O_4@NC-*T* samples of Co 2p Signal

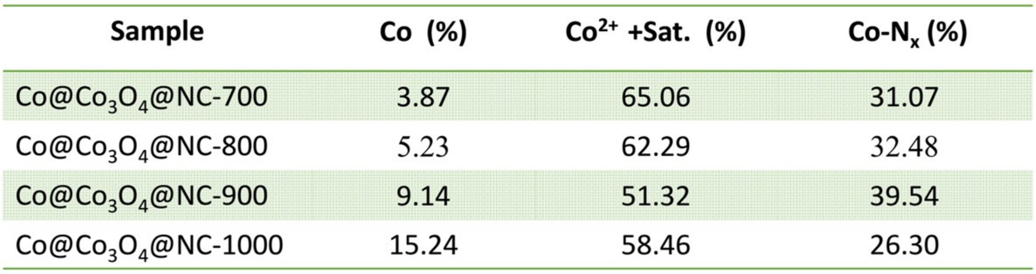

Sample	Co (%)	Co^{2+} +Sat. (%)	Co-N_x (%)
Co@Co_3O_4@NC-700	3.87	65.06	31.07
Co@Co_3O_4@NC-800	5.23	62.29	32.48
Co@Co_3O_4@NC-900	9.14	51.32	39.54
Co@Co_3O_4@NC-1000	15.24	58.46	26.30

As summarized in **Table S3**, Co^{2+} and Co $2P_{3/2}$ satellite (denoted as "sat.") representing Co_3O_4 species is dominant for all Co@Co_3O_4@NC-*T* samples. In addition, concerning the content of Co phase, the following trend is obtained: Co@Co_3O_4@NC-700 < Co@Co_3O_4@NC-800 < Co@Co_3O_4@NC-900 < Co@Co_3O_4@NC-1000 (**Table S3**). Moreover, the percent of CoN_x moieties in total Co element which are the highly active sites for ORR is the highest in Co@Co_3O_4@NC-900 (39.54 %), suggesting that the optimized heating temperature is 900 °C for the formation of CoN_x active sites.

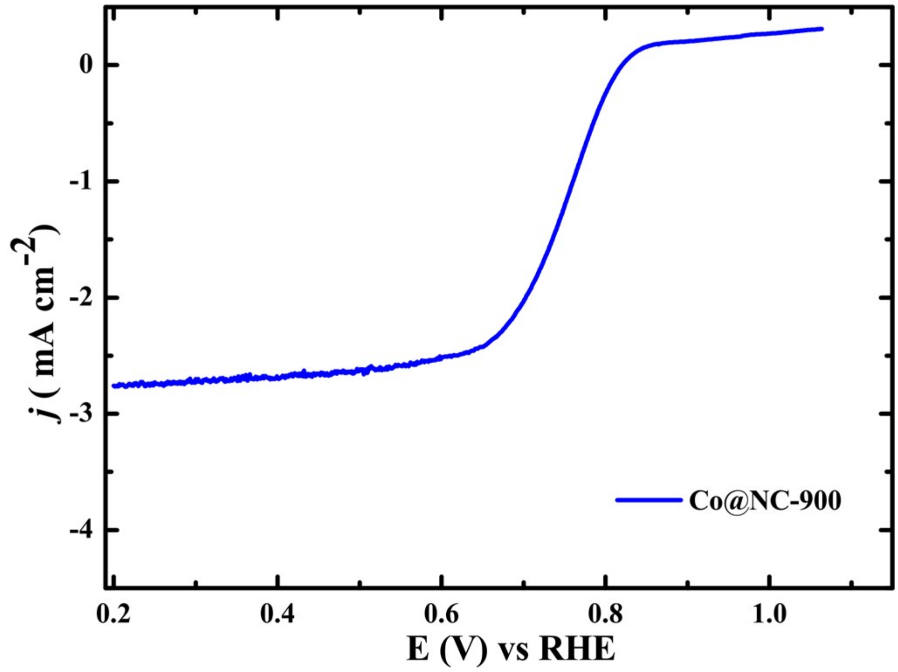

Figure S10 LSV curves of Co@NC-900 for ORR catalytic activity in O_2–saturated 0.1 M KOH solution with a RDE (1600 rpm).

As shown in **Figure S10**, both the limiting current (~2.75 mA cm^{-2}) and half-wave potential (0.75 V) of Co@NC-900 are much lower than these of Co@Co_3O_4@NC-900 (**Figure 5b**), further suggesting that the Co_3O_4 coating layer can effectively enhance the ORR activity of Co@Co_3O_4@NC-900.

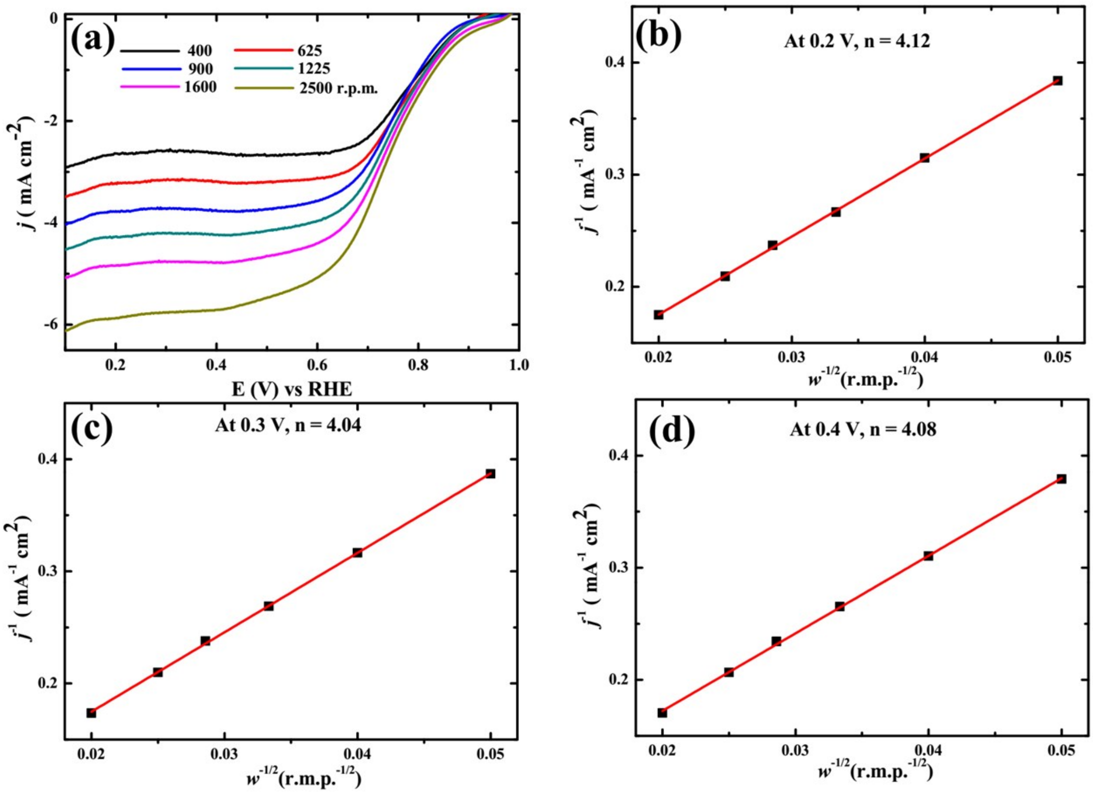

Figure S11 (a) Linear scan voltammogram (LSV) curves for Co@Co_3O_4@NC-900 in O_2-saturated 0.1 M KOH solution at various rotating speeds, scan rate: 5mV s^{-1}; K–L plots for Co@Co_3O_4@NC-900 at various potentials: (b) 0.2 V; (c) 0.3 V; (d) 0.4 V.

As shown in **Figure S11a**，RDE measurements were performed at various rotation rates between 400 to 2500 rpm to understand the ORR kinetics of Co@Co_3O_4@NC-900. The corresponding Koutecky–Levich (K–L) plots are given in **Figure S11b~d**. The linearity and near parallelism of the fitting lines suggest a first-order reaction kinetics towards the concentration of dissolved O_2 for Co@Co_3O_4@NC-900 and similar electron transfer number (n) for ORR within a relatively wide electrochemical window. From the K–L equation, the n was calculated to be approximately 4.0 at the potentials between 0.2 to 0.4 V *vs* RHE (see experimental section for the details), suggesting a 4-electron transfer process for Co@Co_3O_4@NC-900.

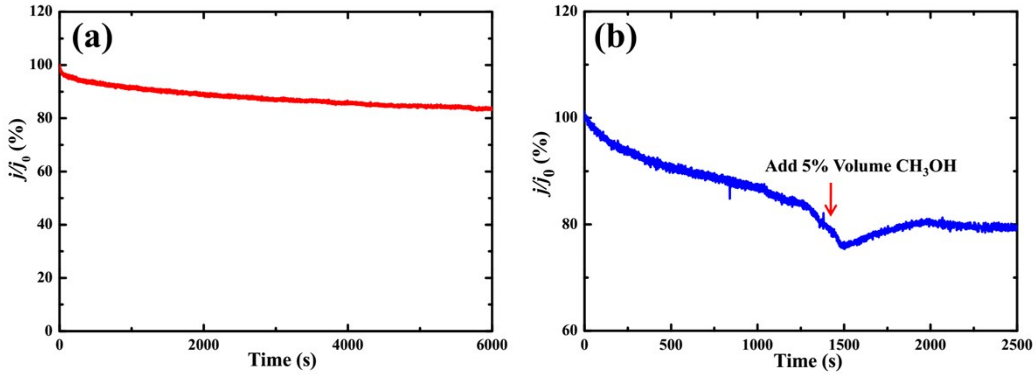

Figure S12 (a) ORR chronoamperometric response of Pt/C in oxygen-saturated 0.1 M KOH at a rotating speed of 1600 rpm and (b) ORR chronoamperometric response after methanol addition. The arrow indicates the addition of 5 % volume methanol into the electrochemical cell.

The durability of catalysts is another crucial parameter for ORR which is very important for the long-term operation in metal–air batteries. Therefore, the chronoamperometric response of Co@Co_3O_4@NC-900 is carried out in oxygen-saturated 0.1 M KOH, compared with that of Pt/C. As shown in **Figure 5c**, the Co@Co_3O_4@NC-900 catalyst can keep about 100% of its initial ORR current density even after 8000 s, while the ORR current loss of Pt/C electrode can reach 17 % only after 6000s (**Figure S12a**), demonstrating the superior stability of Co@Co_3O_4@NC-900 over Pt/C catalyst. Moreover, the methanol-tolerance ability of Co@Co_3O_4@NC-900 is also examined as compared to Pt/C. It can be seen from **Figure 5d** that there is no obvious change for the current density of Co@Co_3O_4@NC-900 to the addition of methanol, whereas a distinct decrease of the current density was occurred after methanol introduction in the case of Pt/C (**Figure S12b**), indicating that Co@Co_3O_4@NC-900 has strong tolerance to methanol crossover.

Table S4 Summary of various electrocatalysts for OER

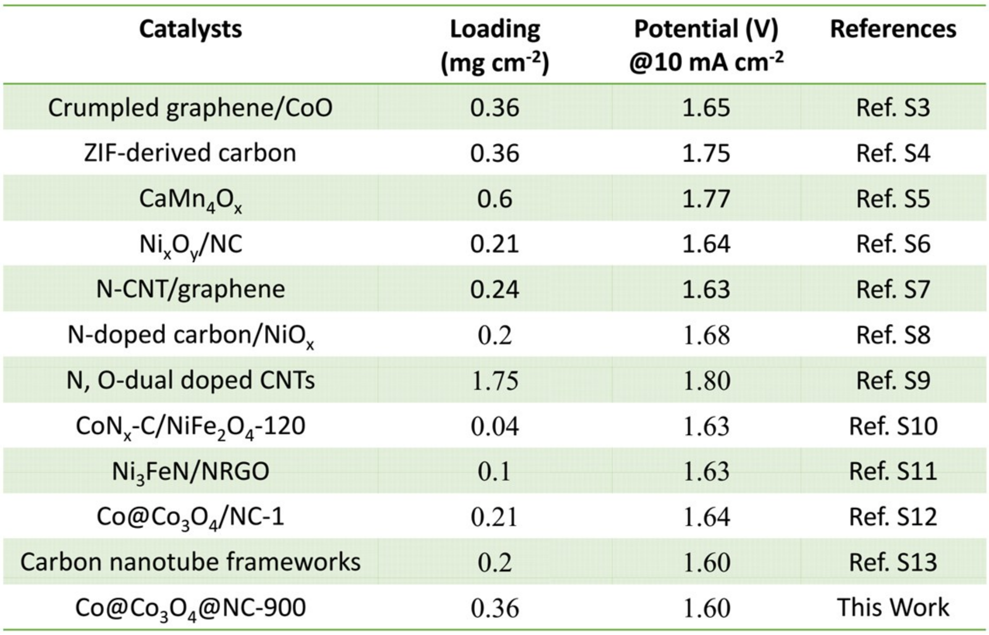

Catalysts	Loading (mg cm^{-2})	Potential (V) @10 mA cm^{-2}	References
Crumpled graphene/CoO	0.36	1.65	Ref. S3
ZIF-derived carbon	0.36	1.75	Ref. S4
$CaMn_4O_x$	0.6	1.77	Ref. S5
Ni_xO_y/NC	0.21	1.64	Ref. S6
N-CNT/graphene	0.24	1.63	Ref. S7
N-doped carbon/NiO_x	0.2	1.68	Ref. S8
N, O-dual doped CNTs	1.75	1.80	Ref. S9
CoN_x-C/$NiFe_2O_4$-120	0.04	1.63	Ref. S10
Ni_3FeN/NRGO	0.1	1.63	Ref. S11
Co@Co_3O_4/NC-1	0.21	1.64	Ref. S12
Carbon nanotube frameworks	0.2	1.60	Ref. S13
Co@Co_3O_4@NC-900	0.36	1.60	This Work

As listed in **Table S4**, Co@Co_3O_4@NC-900 catalyst displays a OER potential of 1.60 V vs.RHE at 10 mA cm^{-2}, which outperform most of the reported catalysts in the recent literatures (**ref. S3-13**), further confirming the superior electrochemical OER performance of Co@Co_3O_4@NC-900.

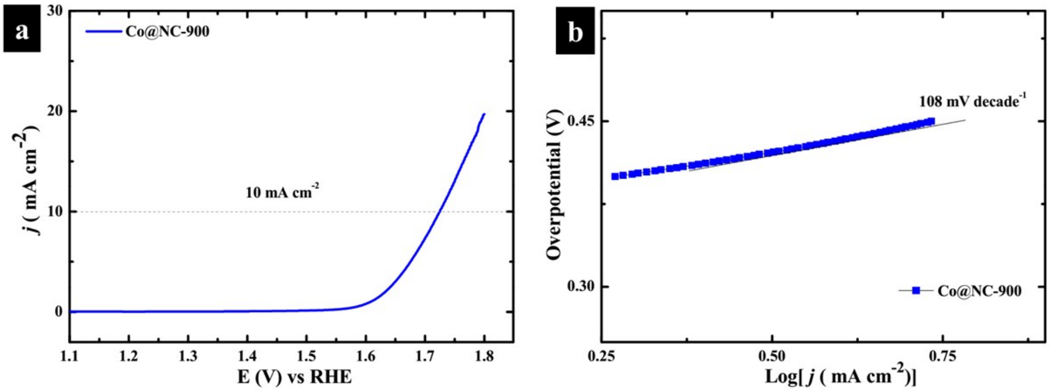

Figure S13 (a) OER polarization curves and (b) the corresponding Tafel plot of Co@NC-900 in 1 M KOH solution with a RDE (1600 rpm).

As shown in **Figure S13**, both the OER potential at 10 mA cm^{-2} and Tafel slope of Co@NC-900 are much higher than these of Co@Co_3O_4@NC-900 (**Figure 5e** and **f**), which further indicates that the Co_3O_4 coating layer can also obviously improve the OER activity of Co@Co_3O_4@NC-900.

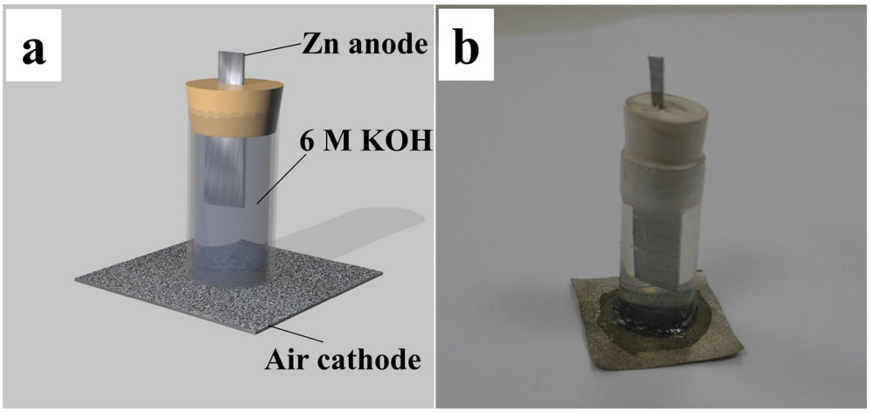

Figure S14 (a) Schematic illustration and (b) Photo profile of a home-made bulk Zn-air battery.

Table S5 Summary of various electrocatalysts for the rechargeable Zn–air batteries

Catalysts	Total Cycle Time (minute)	$E_{overpotential}$ (V)	References
BSCF	1000	0.75@10 mA cm^{-2}	Ref. S14
CoMnO	1033	0.76@10 mA cm^{-2}	Ref. S15
NCNT/CoO-NiO-NiCo	1020	1.05@20 mA cm^{-2}	Ref. S16
NPMC-1000	6000	1.00@2 mA cm^{-2}	Ref. S17
A-EPC-900	9600	0.85@2 mA cm^{-2}	Ref. S18
HMC	1000	0.90@2 mA cm^{-2}	Ref. S19
MCF/N-rGO	300	1.20@10 mA cm^{-2}	Ref. S20
CMS/BNC	1260	0.75@20 mA cm^{-2}	Ref. S21
Ni_3Mn_1 LDHs	5500	0.75@10 mA cm^{-2}	Ref. S22
RuO_2-coated MCNAs	9600	0.80@2 mA cm^{-2}	Ref. S23
$Co_3FeS_{1.5}(OH)_6$	2160	0.75@2 mA cm^{-2}	Ref. S24
Co@Co_3O_4@NC-900	12000	0.66@5 mA cm^{-2}	This Work

As listed in **Table S5**, Co@Co_3O_4@NC-900 catalyst based Zn–air battery shows the lower overpotential and longer cycling time than other bifunctional catalysts based Zn–air batteries in the recent literatures (**ref. S14-24**), which further highlights the superior performance and stability of Co@Co_3O_4@NC-900 for Zn–air cells.

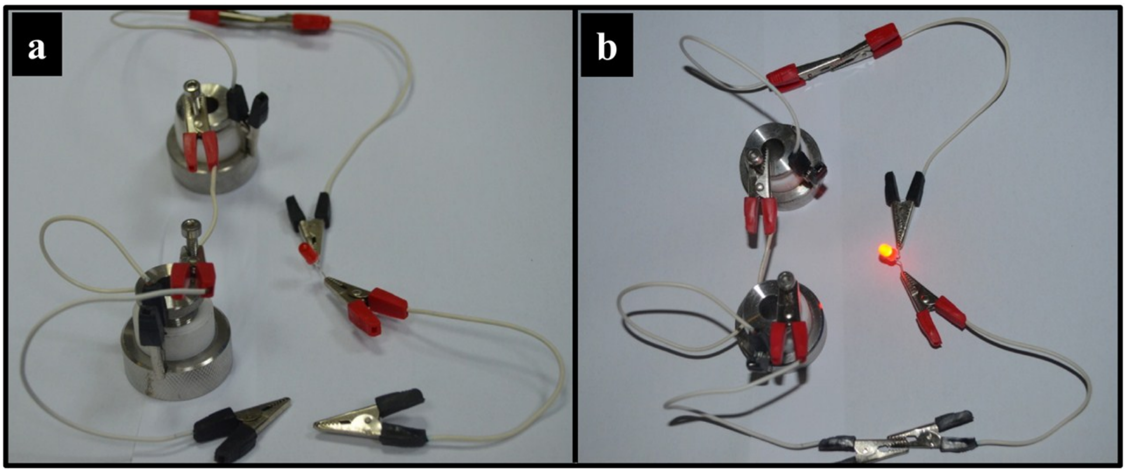

Figure S15 Optical images of an LED (a) before and (b) after being driven by two Zn–air batteries in series (a metallic Zn anode, a catalytic cathode and 6 M KOH electrolyte were sealed into the commercial swagelok cells for photograph).

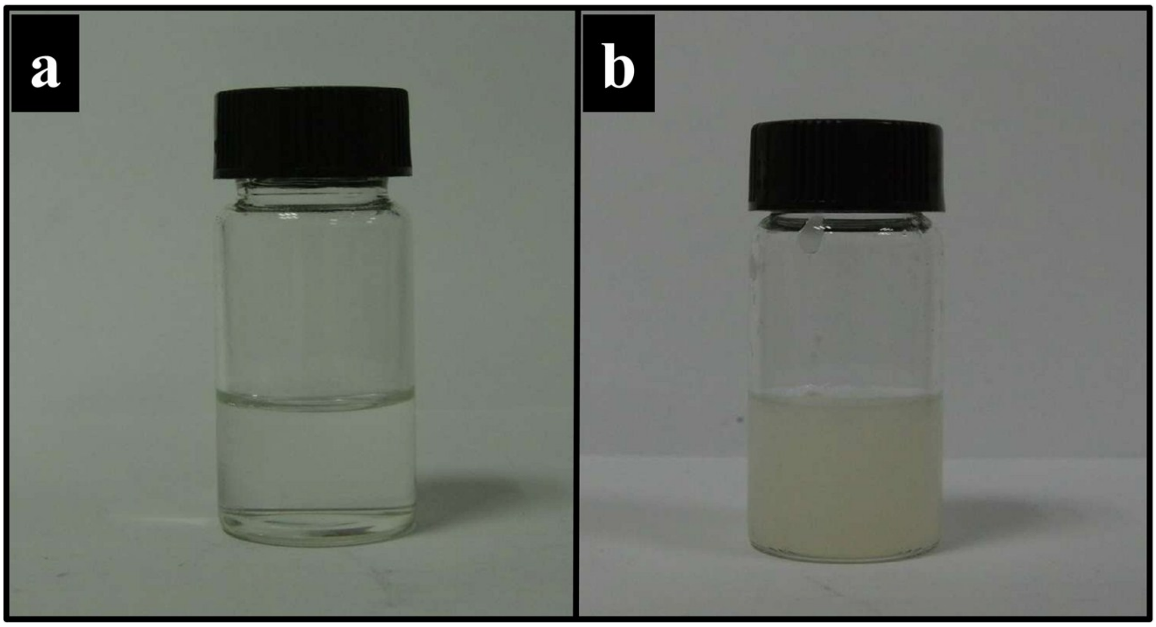

Figure S16 Optical photographs of (a) 6 M KOH solution and (b) the hydrogel polymer electrolyte of poly (vinyl alcohol)-KOH.

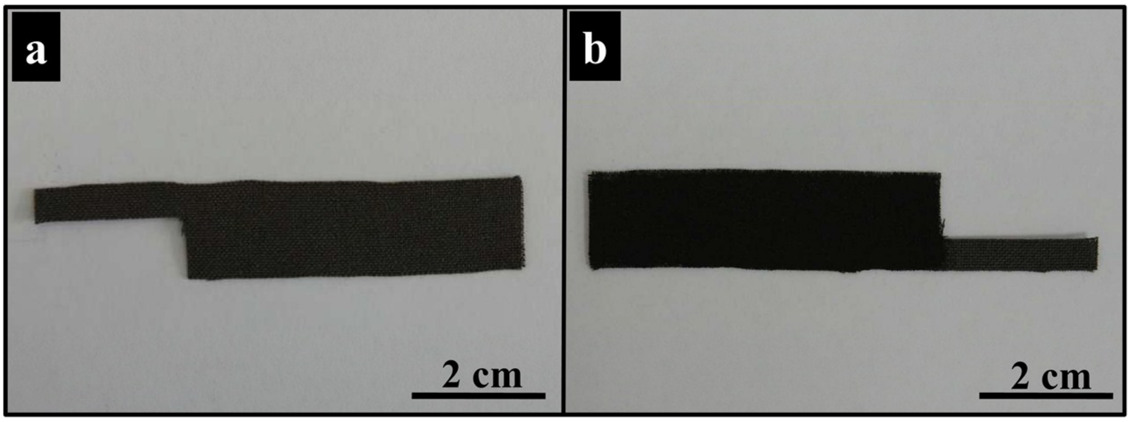

Figure S17 Photo profiles of (a) carbon textiles and (b) Co@Co_3O_4@NC-900/carbon textiles cathode.

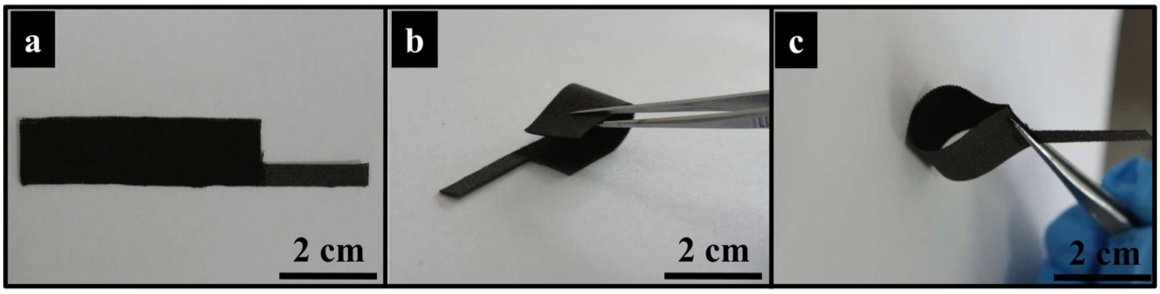

Figure S18 Photo images of Co@Co_3O_4@NC-900 based cathode at different bending conditions.

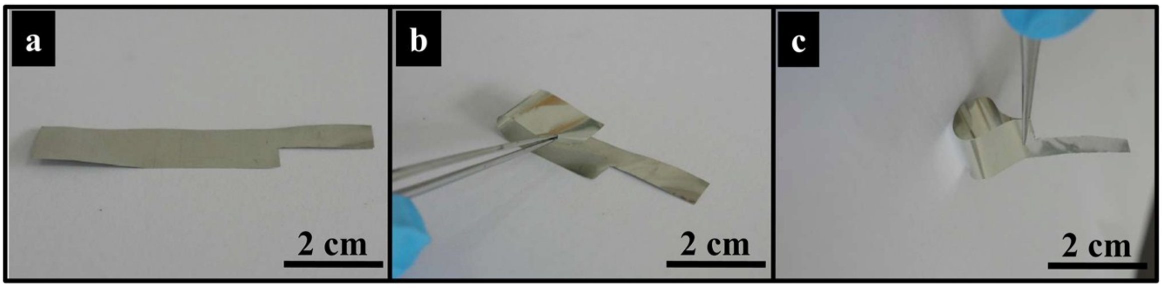

Figure S19 Photo images of Zn anode at different bending conditions.

As shows in **Figure S18** and **19**, both the Co@Co_3O_4@NC-900 based cathode and the Zn anode films exhibit superior flexibility and high mechanical strength since they can be bent at different shapes without damage in structure.

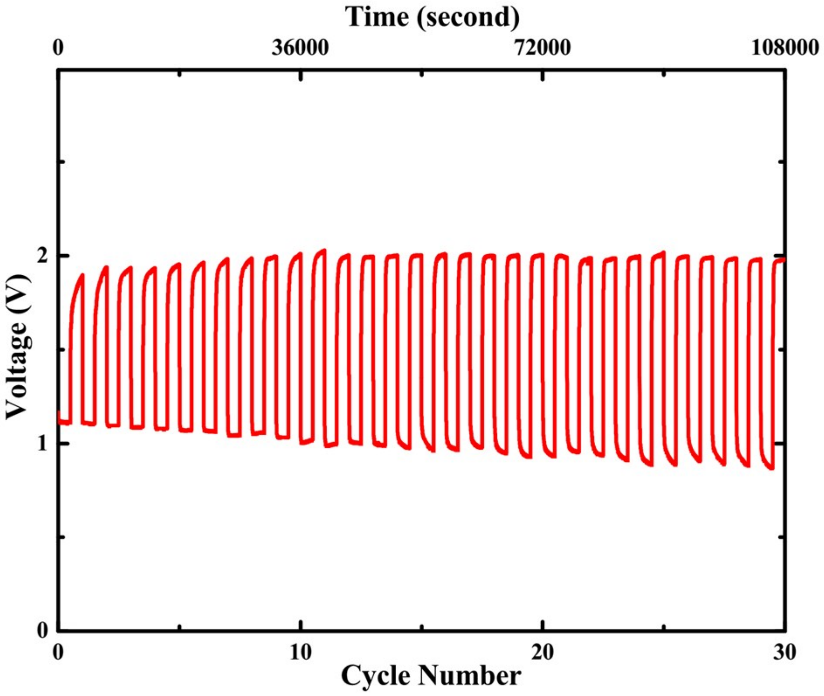

Figure S20 The cycling curves of the belt-shaped Zn–air battery with Co@Co_3O_4@NC-900 catalyst at 1 mA cm^{-2} with 1 h per cycle.

As shown in **Figure S20**, even under the longer time limits, this belt-shaped Zn–air battery can still remain the relatively stable discharge-charge curves over 30 cycles, further demonstrating the good cycle performance of the flexible Zn–air battery with Co@Co_3O_4@NC-900 catalyst.

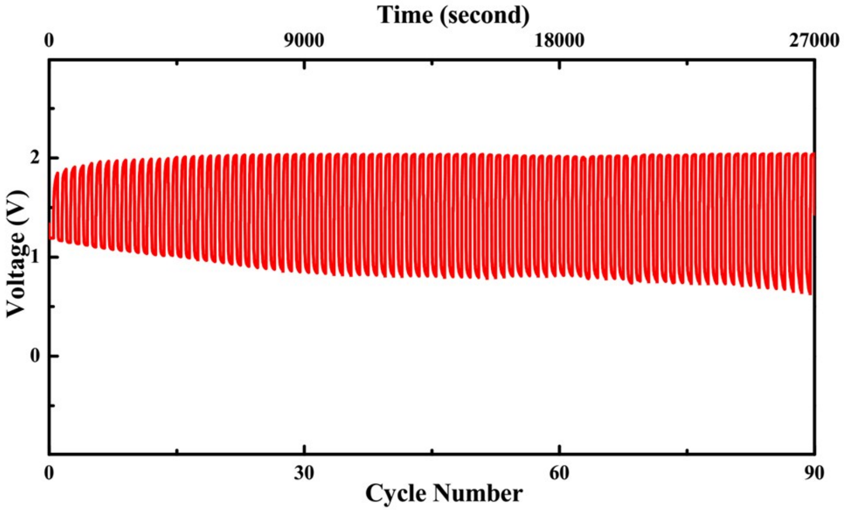

Figure S21 The cycle performance of the belt-shaped Zn–air battery with Co@Co_3O_4@NC-900 catalyst at 5 mA cm^{-2} with a cycle period of 300 s.

As shown in **Figure S21**, even at the higher current density, this battery can still remain the relatively stable voltage curves, except for small increase in voltage polarization during the last 20 cycles, further demonstrating the good cycle performance of the flexible Zn–air battery with Co@Co_3O_4@NC-900 catalyst.

References

ref. S1: Y. Y. Liang, H. L. Wang, J. G. Zhou, Y. G. Li, J. Wang, T. Regier, H. J. Dai, *J. Am. Chem. Soc.* **2012**, *134*, 3517-3523.

ref. S2: Y. H. Deng, C. Liu, T. Yu, F. Liu, F. Q. Zhang, Y. Wan, L. J. Zhang, C. C. Wang, B. Tu, P. A. Webley, H. T. Wang, D. Y. Zhao, *Chem. Mater.* **2007**, *19*, 3271-3277.

ref. S3: S. Mao, Z. H. Wen, T. Z. Huang, Y. Hou, J. H. Chen, *Energy Environ. Sci.* **2014**, *7*, 609-616.

ref. S4: Y. Hou, Z. H. Wen, S. M. Cui, S. Q. Ci, S. Mao, J. H. Chen, *Adv. Funct. Mater.* **2014**, *24*, 5956-5961.

ref. S5: Y. Gorlin, T. F. Jaramillo, *J. Am. Chem. Soc.* **2010**, *132*, 13612-13614.

ref. S6: J. Masa, W. Xia, I. Sinev, A. Zhao, Z. Y. Sun, S. Grützke, P. Weide, M. Muhler, W. Schuhmann, *Angew. Chem. Int. Ed.* **2014**, *53*, 8508-8512.

ref. S7: G. -L. Tian, M. -Q. Zhao, D. S. Yu, X. -Y. Kong, J. -Q. Huang, Q. Zhang, F. Wei, *Small*, **2014**, *10*, 2251-2259.

ref. S8: Y. Zhao, R. Nakamura, K. Kamiya, S. Nakanishi, K. Hashimoto, *Nat. Commun.* **2013**, *4*, 2390.

ref. S9: S. Chen, J. J. Duan, M. Jaroniec, S. -Z. Qiao, *Adv. Mater.* **2014**, *26*, 2925-2930.

ref. S10: H. H. Zhong, R. Tian, D. Q. Li, P. G. Tang, N. Alonso-Vante, Y. J. Feng, *J. Electrochem. Soc.* **2017**, *164*, F491-F498.

ref. S11: Y. Fan, S. Ida, A. Staykov, T. Akbay, H. Hagiwara, J. Matsuda, K. Kaneko, T. Ishihara, *Small*, **2017**, *13*, 1700099.

ref. S12: A. Aijaz, J. Masa, C. Rösler, W. Xia, P. Weide, A. J. R. Botz, R. A. Fischer, W. Schuhmann, M. Muhler, *Angew. Chem. Int. Ed.* **2016**, *55*, 4087-4091.

ref. S13: B. Y. Xia, Y. Yan, N. Li, H. B. Wu, X. W. Lou, X. Wang, *Nat. Energy* **2016**, *1*, 15006.

ref. S14: J. Jung, M. Risch, S. Park, M. G. Kim, G. Nam, Y. Jeong, Y. Shao-Horn, J. Cho, *Energy Environ. Sci.* **2016**, *9*, 176–183.

ref. S15: C. Li, X. P. Han, F. Y. Cheng, Y. X. Hu, C. C. Chen, J. Chen, *Nat. Commun.* **2015**, *6*, 7345.

ref. S16: X. Liu, M. Park, M. G. Kim, S. Gupta, G. Wu and J. Cho, *Angew. Chem. Int. Ed.*, **2015**, *54*, 9654-9658.

ref. S17: J. T. Zhang, Z. H. Zhao, Z. H. Xia, L. M. Dai, *Nat. Nanotechnol.* **2015**, *10*, 444-452.

ref. S18: B. Li, D. S. Geng, X. S. Lee, X. M. Ge, J. W. Chai, Z. J. Wang, J. Zhang, Z. L. Liu, T. S. A. Hor, Y. Zong, *Chem. Commun.* **2015**, *51*, 8841-8844.

ref. S19: L. Hadidi, E. Davari, M. Iqbal, T. K. Purkait, D. G. Ivey, G. C. Veinot, *Nanoscale* **2015**, *7*, 1830-1838.

ref. S20: Y. Zhan, C. Xu, M. Lu, Z. Liu, J. Y. Lee, *J. Mater. Chem. A*, **2014**, *2*, 16217-16223.

ref. S21: Z. Wang, S. Xiao, Y. An, X. Long, X. L. Zheng, X. H. Lu, Y. X. Tong, S. H. Yang, *ACS Appl. Mater. Interfaces* **2016**, *8*, 13348-13359.

ref. S22: A. Sumboja, J. W. Chen, Y. Zong, P. S. Lee, Z. L. Liu, *Nanoscale* **2017**, *9*, 774-780.

ref. S23: Z. Y. Guo, C. Li, W. Y. Li, H. Guo, X. L. Su, P. He, Y. G. Wang, Y. Y. Xia, *J. Mater. Chem. A* **2016**, *4*, 6282-6289.

ref. S24: H. -F. Wang, C. Tang, B. Wang, B. -Q. Li, Q. Zhang, *Adv. Mater.* **2017**, *DOI: 10.1002/adma.201702327*.